



Tunable stacking fault energies by tailoring local chemical order in CrCoNi medium-entropy alloys

Jun Ding^a, Qin Yu^a, Mark Asta^{a,b,1}, and Robert O. Ritchie^{a,b,1}

^aMaterials Sciences Division, Lawrence Berkeley National Laboratory, Berkeley, CA 94720; and ^bDepartment of Materials Science & Engineering, University of California, Berkeley, CA 94720

Edited by William D. Nix, Stanford University, Stanford, CA, and approved July 25, 2018 (received for review May 20, 2018)

High-entropy alloys (HEAs) are an intriguing new class of metallic materials due to their unique mechanical behavior. Achieving a detailed understanding of structure–property relationships in these materials has been challenged by the compositional disorder that underlies their unique mechanical behavior. Accordingly, in this work, we employ first-principles calculations to investigate the nature of local chemical order and establish its relationship to the intrinsic and extrinsic stacking fault energy (SFE) in CrCoNi medium-entropy solid-solution alloys, whose combination of strength, ductility, and toughness properties approaches the best on record. We find that the average intrinsic and extrinsic SFE are both highly tunable, with values ranging from -43 to 30 $\text{mJ}\cdot\text{m}^{-2}$ and from -28 to 66 $\text{mJ}\cdot\text{m}^{-2}$, respectively, as the degree of local chemical order increases. The state of local ordering also strongly correlates with the energy difference between the face-centered cubic (*fcc*) and hexagonal close-packed (*hcp*) phases, which affects the occurrence of transformation-induced plasticity. This theoretical study demonstrates that chemical short-range order is thermodynamically favored in HEAs and can be tuned to affect the mechanical behavior of these alloys. It thus addresses the pressing need to establish robust processing–structure–property relationships to guide the science-based design of new HEAs with targeted mechanical behavior.

medium-entropy alloys | local chemical order | stacking fault energy | transformation-induced plasticity

High-entropy alloys (HEAs), also referred to as multiprincipal element alloys, have emerged as an exciting new class of metallic structural materials. These alloys are, in principle, single-phase crystalline solid solutions comprising multiple elements, typically in equal molar ratios (1–5). The original rationale guiding the discovery of HEAs was that the configurational entropy contribution to the total free energy in multicomponent concentrated alloys can stabilize the solid-solution state relative to a multiphase microstructure composed of chemically ordered intermetallic phases (1, 2). Currently, HEAs are attracting extensive research interest because some of these systems, in particular those based on the face-centered cubic (*fcc*) CrCoNi system, have been found to display excellent mechanical properties, including very high fracture toughness and high strength (6, 7). The five-element (so-called Cantor) HEA, CrMnFeCoNi, was the first to be shown to exhibit exceptional damage tolerance, which can be further enhanced at cryogenic temperatures (6). Additionally, the equiatomic, three-element (medium-entropy) CrCoNi alloy has been observed to display even better properties; at 77 K, this alloy displays tensile strengths of 1.4 GPa, tensile ductilities of $\sim 90\%$, and fracture toughness values of $275 \text{ MPa}\sqrt{\text{m}}$, approaching the best damage tolerance on record (7). A synergy of deformation mechanisms appears to be the basis of the exceptional mechanical behavior of these alloys (8–13). For instance, in the stronger medium-entropy CrCoNi alloy, nanotwinning occurs at room temperature and leads to the formation of a hierarchical twin network, where the twin boundaries act as barriers to dislocation motion, providing for strength, whereas both full and partial dislocations can move rapidly along the boundaries themselves for

ductility (11). Additionally, a lamellar hexagonal close-packed (*hcp*) phase has been reported to form in this alloy at higher strain levels (13).

Such unique mechanical behavior for the CrCoNi and CrMnFeCoNi alloys appears to be associated with their low stacking fault energies (SFE) because the SFE is one of the most significant parameters influencing plastic deformation, dislocation mobility, and deformation twinning as well as occurrence of phase transformations in conventional crystalline alloys (14–16) (*SI Appendix, SI Text*). For the CrCoNi alloy, experimental measurements of the separation of partial dislocations suggested values of the SFE of $22 \pm 4 \text{ mJ}\cdot\text{m}^{-2}$ (9); conversely, first-principles density functional theory (DFT) calculations have yielded negative values of the SFE for this alloy, e.g., $-24 \text{ mJ}\cdot\text{m}^{-2}$ (11), $-62 \text{ mJ}\cdot\text{m}^{-2}$ (17), or $-41 \text{ mJ}\cdot\text{m}^{-2}$ (18), which are apparently at odds with the measured finite dislocation dissociation widths. Given the importance of the SFE in governing the nanoscale mechanisms active during plastic deformation, this discrepancy between measurement and computation clearly warrants further investigation.

The unique properties of HEAs mainly originate from their multiple components and special chemical structure, compared with conventional crystalline alloys. In HEAs, the atomic structure is characterized by an underlying crystal lattice [e.g., *fcc*, *bcc* (body-centered cubic), or *hcp*] but with atoms of different elements occupying the sites of the lattice in a nonperiodic manner. The distribution of heterogeneous local environments in HEAs should be different from that of metallic glasses (19) and conventional crystalline alloys (*SI Appendix, Fig. S1*). In the simplest description, the local chemical environments of HEAs can be considered as representing a random distribution of different atomic species over crystal lattice sites, i.e., the maximum configurational entropy state (1). However, as has been discussed in

Significance

Our work has revealed the nature of local chemical order and has established its significant relationship to the intrinsic and extrinsic stacking fault energy in CrCoNi medium-entropy solid-solution alloys, whose combination of strength, ductility, and toughness properties approaches the best on record. These findings highlight the general need to discern how critical the role of local chemical ordering is in dictating the mechanical properties of medium- and high-entropy alloys. Our results highlight the possibility of tuning order in disorder to ultimately achieve the science-based design and optimization of new high-entropy alloy systems with specifically desired combinations of macroscale mechanical properties.

Author contributions: J.D., M.A., and R.O.R. designed research; J.D. and Q.Y. performed research; J.D. analyzed data; and J.D., M.A., and R.O.R. wrote the paper.

The authors declare no conflict of interest.

This article is a PNAS Direct Submission.

Published under the PNAS license.

¹To whom correspondence may be addressed. Email: mdasta@berkeley.edu or roritche@lbl.gov.

This article contains supporting information online at www.pnas.org/lookup/suppl/doi:10.1073/pnas.1808660115/-DCSupplemental.

Published online August 20, 2018.

from a random solid solution, compared with the other five pair types). Following the trend in the energy shown in Fig. 1A, the evolution in the local chemical order is initially rapid but then becomes more gradual at the later stages of the simulation. As is commonly observed for chemical short-range ordering in alloys, contrasting behavior is obtained for nearest-neighbor and further-neighbor shells; as shown in Fig. 1C, the number of Cr–Cr pairs is reduced in the first nearest-neighbor shell of Cr atoms, whereas the second and third nearest-neighbor shells show an enhancement.

For the final state of the MC simulation (*CH_F*), the local chemical order, averaged over the 18 independent samples, is plotted in Fig. 1D, in terms of the values of $\Delta\delta_{ij}^k$ for $ij = \text{Cr–Cr, Cr–Co, Cr–Ni, Co–Co, Co–Ni, and Ni–Ni}$ pairs at the first three nearest-neighbor shells. The dashed lines represent the case of a random solid solution. Deviations from random behavior are clearly evident. As discussed above, the most pronounced local chemical ordering is around Cr atoms. Specifically, for the nearest-neighbor shell, $\Delta\delta_{\text{Cr–Cr}}^1$ is about 1.58, whereas $\Delta\delta_{\text{Cr–Co}}^1 \approx -0.98$ and $\Delta\delta_{\text{Cr–Ni}}^1 \approx -0.61$, as seen in Fig. 1D. The general trend related to chemical order for Cr–Cr pairs is consistent with previous DFT-MC simulations (20) and also with EXAFS analysis (21), as described above. The chemical order around Cr atoms is still significant for the second and third nearest-neighbor shells but with the opposite trend to that for nearest neighbors (i.e., an enhancement in Cr atoms and depletion in Ni and Co atoms around a central Cr, as shown in Fig. 1D). Similar trends are also observed for the chemical ordering around Co and Ni atoms. We note that our calculation indicates a slight preference for Ni–Ni pairs in the first nearest-neighbor shell, which is contrary to the findings in ref. 20, where a slightly smaller simulation cell and lower degree of Monte Carlo sampling was employed.

Stacking Fault Energy of Random Solid-Solution CrCoNi Alloys. In the DFT calculations of the SFE for both intrinsic stacking faults (*ISF*) and extrinsic stacking faults (*ESF*) as illustrated in Fig. 2A–D, we consider slabs containing 360 atoms created by sequentially stacking 12 close-packed (111) atomic planes in their regular *ABCABCABCABC* configuration. An *ISF* was created by shifting the top six layers along the $\langle 11\bar{2} \rangle$ direction by the Burgers vector of the Shockley partial $b_s = \frac{a}{6} \langle 11\bar{2} \rangle$; this results in a stacking sequence: *ABCABC|BCABCA*. Further shifting of the fault leads to the *ESF*, as shown in Fig. 2C, resulting in a stacking sequence of *ABCABC|B|ABCAB*. The value of γ_{isf} and γ_{esf} was obtained from the energy difference between the original and stacking faulted structures, normalized by the corresponding area. Further details are given in *Methods*.

For the CrCoNi alloys with random compositional disorder, 108 independent as-assigned supercells were considered in total; the resulting calculated values of γ_{isf} are shown in Fig. 2E, *Inset*. The calculated values of γ_{isf} display a large range, from -140 to $65 \text{ mJ}\cdot\text{m}^{-2}$, with an average value of $-42.9 \text{ mJ}\cdot\text{m}^{-2}$, as shown in Fig. 2E. In addition, the average value of γ_{esf} is about $-27.8 \text{ mJ}\cdot\text{m}^{-2}$, which is also negative but with a smaller magnitude than $\bar{\gamma}_{\text{isf}}$. By comparison, additional values of γ_{isf} were computed using replicated configurations from the smaller random solid-solution models described in the previous section on MC simulations (see *Methods* for details of replication). For each replicated sample, all of the six close-packed atomic planes were considered, and again, 18 independent samples having in total 108 ISF planes were considered. The corresponding $\bar{\gamma}_{\text{isf}}$ values are plotted in Fig. 2E. These replicated samples lead to values close to those for the as-assigned supercells. This result provides validation for our calculation of SFE using the replicated configurations, which forms the basis for the studies, described in the next section below, of the effects of chemical SRO on SFE.

The magnitude of $\bar{\gamma}_{\text{isf}}$ calculated here, $-42.9 \text{ mJ}\cdot\text{m}^{-2}$, differs from previously published values of $-24 \text{ mJ}\cdot\text{m}^{-2}$ (11), $-62 \text{ mJ}\cdot\text{m}^{-2}$ (17), $-41 \text{ mJ}\cdot\text{m}^{-2}$ (18), and $-48 \text{ mJ}\cdot\text{m}^{-2}$ (25) that were also calculated using supercell methods. We view these differences with

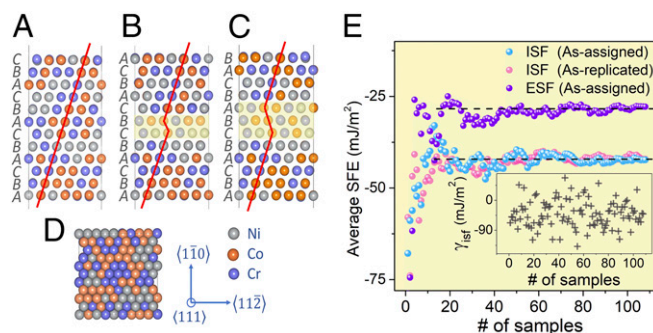


Fig. 2. Calculated stacking fault energy of the random solid-solution CrCoNi alloys. (A–C) The side view images of atomic configurations in the original *fcc* structure, with *ISF* and *ESF*. The yellow shade indicates the stacking fault; the plane labels of *ABC...* represent the sequence of close-packed (111) planes. (D) Top view image showing the close-packed (111) plane. (E) The average SFE with the number of random solid-solution CrCoNi samples (containing 360 atoms each) for both as-assigned and replicated supercells (*Methods*). (*Inset*) The γ_{isf} of as-assigned supercells of CrCoNi alloys.

our present value as reflecting the need, as illustrated in Fig. 2E, for a large number of samples to achieve well-converged averaged results (only limited configurations were considered in refs. 11, 17, and 25). Other DFT calculations, using the coherent potential approximation (CPA) or axial interaction model, yielded SFE values of $-26 \text{ mJ}\cdot\text{m}^{-2}$ (26) and $-25 \text{ mJ}\cdot\text{m}^{-2}$ (17), respectively. Despite these quantitative differences, the finding of negative $\bar{\gamma}_{\text{isf}}$ values for CrCoNi alloys with random configurational disorder is robust across all previous DFT calculations. As described above, this finding is at odds with experimental measurements, clearly warranting further examination. In the next section, the effect of local chemical ordering is considered, with the main finding that such chemical SRO is capable of leading to a change in sign of the SFE.

Stacking Fault Energy Strongly Correlates with Local Chemical Order.

Fig. 2, *Inset*, shows a wide range of calculated γ_{isf} values for random CrCoNi solid solutions, which is in contrast to a single value for a pure or perfectly ordered crystalline alloy. A similar broad distribution can also be observed for CrCoNi alloys with chemical SRO (Fig. 3A). As plotted in Fig. 3A, the statistical variations of the calculated γ_{isf} for four groups of configurations all follow Gaussian-type distributions. The mean value for CrCoNi alloys in *CH 0*, *CH 1*, *CH 2*, and *CH F* have been computed to be -42.9 , -13.9 , 13.3 , and $30.0 \text{ mJ}\cdot\text{m}^{-2}$, respectively. The results establish a trend of increasing values of the SFE with increasing degree of chemical SRO. In contrast, the widths of the distributions (with the SD of $\sim 31 \text{ mJ}\cdot\text{m}^{-2}$) are almost unchanged for varying states of chemical SRO. Although the exact width of the distributions depends on the size of the supercell used in the calculations, the results clearly illustrate how variations in the local composition and order affect planar fault energies. We note that a heterogeneous distribution of local SFE may affect the plastic deformation mechanisms, considering the existence of both weak and strong close-packed atomic planes that is in contrast with conventional crystalline alloys. A similar example can be found in studying the dislocation cross-slip affected by the fluctuations in the spatial solute distribution in random solid solutions (27).

The average SFE, $\bar{\gamma}_{\text{isf}}$, and $\bar{\gamma}_{\text{esf}}$ in CrCoNi alloys can be quantitatively correlated with the degree of chemical SRO, reflected by the total nonproportional number of local atomic pairs, $\Delta\delta_{\text{sum}}$, as shown in Fig. 3B and C, respectively. Such a relationship can be understood as reflecting the effect of the stacking fault-induced disruption of local chemical order that increases the energy state of deformed samples. Specifically, in a sample with configurational SRO, the creation of a stacking fault

by shear displacements changes not only the stacking sequence but also the state of order near the stacking fault plane. This latter effect leads to an increase in stacking fault energy that is expected to increase with the magnitude of the SRO, as indicated in Fig. 3. The $\Delta\delta_{sum}$ values, reflecting chemical order summed over all pairs (Methods), are found to exhibit a monotonically linear relationship with the value of $\bar{\gamma}_{isf}$ and $\bar{\gamma}_{esf}$ (Fig. 3 B and C), for the first, second, and third nearest-neighbor shells. By increasing the degree of local chemical order, the value of $\bar{\gamma}_{isf}$ can be tuned remarkably from an average value of -42.9 to 30 $\text{mJ}\cdot\text{m}^{-2}$, whereas the value of $\bar{\gamma}_{esf}$ can be tuned from -27.8 to 66 $\text{mJ}\cdot\text{m}^{-2}$. Such variations, in $\bar{\gamma}_{isf}$ by more than 70 $\text{mJ}\cdot\text{m}^{-2}$ and $\bar{\gamma}_{esf}$ by more than 90 $\text{mJ}\cdot\text{m}^{-2}$, are substantial for a crystalline metal or alloy and would be expected to significantly affect mechanical deformation mechanisms, as described in Discussion and Conclusions.

It is also worth noting that the experimental measured γ_{isf} is 22 ± 4 $\text{mJ}\cdot\text{m}^{-2}$ at 300 K, which already falls within the range explored by our DFT calculation at 0 K in Fig. 3B. In comparing our zero-temperature calculated values with experiment measurements at room temperature, it is important to note that the stacking fault free energies at finite temperature need to consider the entropy contributions from atomic vibrations, magnetism, and electronic excitations (18, 28). In recent work by Niu et al. (18), vibrational free energies were incorporated in the calculation of *hcp*-*fcc* free-energy differences for random CoCrNi alloys, with the finding that the free energies changed by less than 15% in the temperature range between 0 and 300 K. We thus expect that the vibrational contributions to the SFE values will be similarly relatively small over this temperature range in such alloys, and the measured values for SFE in experimental CrCoNi samples extrapolated to 0 K would be slightly smaller than the reported room temperature value of 22 ± 4 $\text{mJ}\cdot\text{m}^{-2}$. This finding appears to imply that the CrCoNi alloys that have been investigated experimentally to date likely possess a significant degree of local chemical SRO, which falls within the

range investigated by our DFT calculation, rather than being a random solid solution.

Occurrence of the *fcc* Versus *hcp* Phase. Understanding the competition of *fcc* and *hcp* phases is critical for CrCoNi solid-solution alloys. First, it is expected that the SFE in *fcc* crystal correlates with the value of $\Delta E^{fcc \rightarrow hcp}$, as the intrinsic stacking fault can be considered as a two-layer embryo of the *hcp* structure embedded in the *fcc* matrix (see, e.g., ref. 29). Second, the as-prepared CrCoNi medium-entropy alloys crystallize as *fcc* solid solutions in experiment, whereas this is seemingly in conflict with previous computational results showing that the *hcp* phase is energetically favored relative to the *fcc* phase (11, 13, 18). Moreover, at large strain levels of deformation in CrCoNi alloys, a new phase with *hcp* lamellae has been reported to appear within the matrix of the *fcc* phase (13). This could be suggestive of a transformation-induced plasticity effect that would be expected to occur if the *hcp* structure has a lower energy than that of the *fcc* phase, which then would be considered to be metastable. More recently, Niu et al. (18) employed DFT calculations, considering the magnetic contribution to the relative phase stability, unique dislocation mechanisms for *fcc* to *hcp* phase transformation, as well as the effects of vibrational entropy (see above) in leading to a transition temperature between these phases assuming random configurational disorder. In light of these considerations, it is very important to investigate the effects of local chemical order on the *hcp*-*fcc* energy difference ($\Delta E^{fcc \rightarrow hcp} = E_{hcp} - E_{fcc}$).

Fig. 4 A and B show the side and top view images, respectively, of atomic configurations of CrCoNi alloys in *fcc* and *hcp* structures. The sequence of close-packed (111) planes changes from *ABCABC* for *fcc* phase to *ABABAB* for *hcp* phase. The relative energies for those two phases in CrCoNi alloys are plotted in Fig. 4C, for four specific states of chemical order. The green shades indicate the corresponding values of $\Delta E^{fcc \rightarrow hcp}$. It should be noted that these calculated values of $\Delta E^{fcc \rightarrow hcp}$ represent the difference in energy between the *fcc* phase with its corresponding equilibrated state of SRO and an *hcp* structure that results by changing the stacking sequence but without reequilibrating the configurational order. The energy difference calculated here is thus intended to correspond to the bulk energy difference between the parent *fcc* phase and an *hcp* nucleus that would form, e.g., through consecutive passage of partial dislocations, at low temperatures where substitutional diffusion is slow and the configurational order can be considered frozen.

The calculated energy differences show that for the random solid solution (*CH_0*), the *hcp* phase is energetically favored, consistent with earlier calculations (18). On increasing the degree of local chemical order, the energies for both phases decrease, but the energy of the *fcc* phase drops faster, as seen in Fig. 4C. At the final state (*CH_F*), the value of $\Delta E^{fcc \rightarrow hcp}$ reverses, favoring the *fcc* phase. The behavior of $\Delta E^{fcc \rightarrow hcp}$ can be quantitatively correlated with $\Delta\delta_{Cr-Cr}^1$, so that it reflects the local chemical order, as shown in Fig. 4C, Inset.

Fig. 4D plots $\bar{\gamma}_{isf}$ versus $\Delta E^{fcc \rightarrow hcp}$ for CrCoNi alloys with varying chemical SRO, and a nearly linear relation is obtained, as theoretically predicted. For the random solid solution, the DFT-calculated negative value of $\Delta E^{fcc \rightarrow hcp}$ correlates with the negative value of $\bar{\gamma}_{SFE}$. Dashed lines in Fig. 4D indicate where $\bar{\gamma}_{isf} = 0$ or $\Delta E^{fcc \rightarrow hcp} = 0$. Of note, where the *hcp* phase is energetically equivalent to the *fcc* phase, the corresponding $\bar{\gamma}_{SFE}$ is predicted to be ~ 18 $\text{mJ}\cdot\text{m}^{-2}$ [two times of the interfacial energy between the *fcc* and *hcp* phases (29)]. In particular, there are states of chemical order that give rise to positive stacking fault energies (consistent with experimental measurements of the SFE in ref. 9) but with very low or even negative values of $\Delta E^{fcc \rightarrow hcp}$. For such alloys, deformation may enable the in situ transformation of *fcc* to *hcp* structures, which can contribute to the steady high strain-hardening rates (13), which in turn are likely to result in both

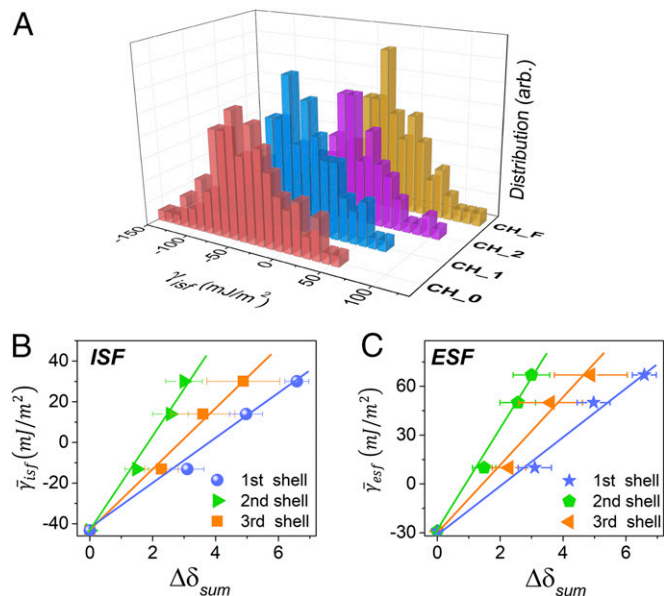


Fig. 3. Stacking fault energy correlates strongly with local chemical ordering. (A) Distribution of intrinsic stacking fault energy, γ_{isf} , for the CrCoNi alloys in four specific states, which span from random solid solution to the highest degree of chemical ordering extracted from the MC simulations. In total, 108 stacking faults were considered for analysis in each group. The average stacking fault energies, (B) $\bar{\gamma}_{isf}$ and (C) $\bar{\gamma}_{esf}$, among those four groups are plotted versus $\Delta\delta_{sum}$ for the first, second, and third nearest-neighbor shells.

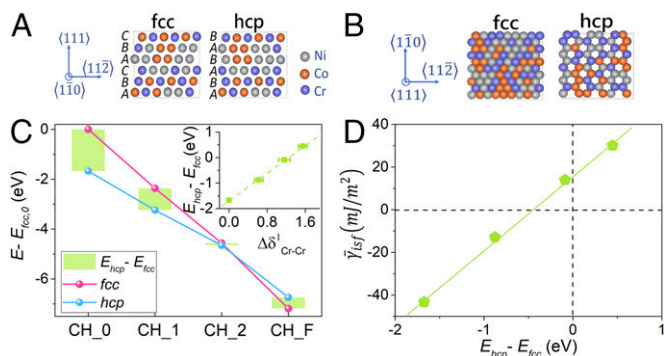


Fig. 4. Energies of *fcc* and *hcp* structures in CrCoNi solid-solution alloys. The (A) side and (B) top view images of atomic configurations for the CrCoNi alloys in both *fcc* and *hcp* phases. (C) The relative energy difference ($E - E_{fcc,0}$) for both *fcc* and *hcp* phase at various degrees of local chemical ordering, where $E_{fcc,0}$ is the average potential energy of the *fcc* CrCoNi alloys with random configurational disorder. (Inset) The correlation between $\Delta\delta^1_{Cr-Cr}$ and energy difference between the *hcp* and *fcc* phases, $\Delta E^{fcc-hcp}$. (D) The correlation between $\bar{\gamma}_{isf}$ and $\Delta E^{fcc-hcp}$. Dashed lines indicate where $\bar{\gamma}_{isf} = 0$ or $\Delta E^{fcc-hcp} = 0$.

high tensile strength and ductility in such alloys, as discussed in *Discussion and Conclusions*.

Therefore, two critical results have been collected for CrCoNi solid-solution alloys: (i) tuning the local chemical order can significantly change the preference between *fcc* and *hcp* phases, from negative $\Delta E^{fcc-hcp}$ to the positive value and (ii) the quantitative relationship between the $\Delta E^{fcc-hcp}$ and SFE can be established for this alloy at various states of local chemical order. Those findings provide new insights to understand the phase stability as well as deformation-induced phase transformation in CrCoNi solid-solution alloys.

Discussion and Conclusions

Stacking fault energies and structural energy differences in CrCoNi solid solutions, as represented by medium-entropy alloys and as a basis for the Cantor CrMnFeCoNi high-entropy alloy, have been studied in this work using DFT calculations, with a specific focus on the effect of local chemical ordering. From MC simulations, we find strong tendencies for the formation of chemical SRO, particularly around Cr atoms, which favor Ni and Co atoms as nearest neighbors, and an enhancement of Cr neighbors in the second and third shells. It is important to emphasize that the state of local chemical order in CrCoNi solid solutions, as well as other HEAs, need not be that corresponding to an equilibrium thermodynamic state, because it is inherited through cooling from high temperatures. This is very significant because it means that not only the microstructure but also the local chemical order can be controlled, e.g., by adjusting the heat treatment at elevated temperatures, to enhance or disfavor the degree of ordering. However, this has yet to be proven experimentally, in part because of the difficulty in assessing regions of chemical order. However, the strong effects of local chemical order on the underlying planar fault and structural energy differences found in this theoretical study emphasize that experimental studies of structure–properties relationships in these multiple-element materials should now involve additional detailed measurements of chemical order. Indeed, this is becoming increasingly feasible through the use of atom probe tomography and advanced transmission electron microscopy techniques (30, 31).

The present calculations, summarized in Fig. 3, demonstrate that the average SFE of CrCoNi solid-solution alloys can vary remarkably as the degree of chemical SRO increases. Specifically, as the degree of chemical SRO is varied from the random configuration up to the highest degree of order realized in the MC simulations, the value of $\bar{\gamma}_{isf}$ increases from -42.9 to 30 $\text{mJ}\cdot\text{m}^{-2}$,

whereas the value of $\bar{\gamma}_{esf}$ ranges between -27.8 and 66 $\text{mJ}\cdot\text{m}^{-2}$. In comparison, the experimentally measured value of $\bar{\gamma}_{isf}$, 22 ± 4 $\text{mJ}\cdot\text{m}^{-2}$, falls within the range explored by our DFT calculation, implying that CrCoNi alloys may contain a degree of local chemical order, although not necessarily the value corresponding to thermodynamic equilibrium at room temperature (because it is inherited from cooling from high temperature). This notion offers a profound resolution to the discrepancy between experimental SFE measurements and previous DFT calculations that have found negative values for the SFE of this alloy. Specifically, in all of the DFT calculations of the SFE of CrCoNi alloys before this work, chemical ordering has not been explicitly accounted for.

The present computational study has revealed four characteristic features of the stacking fault energies in medium-entropy CrCoNi solid-solutions: (i) The average SFE is highly tunable with a substantial variation of more than 70 $\text{mJ}\cdot\text{m}^{-2}$ for $\bar{\gamma}_{isf}$ and more than 90 $\text{mJ}\cdot\text{m}^{-2}$ for $\bar{\gamma}_{esf}$ by tailoring local chemical ordering. (ii) The low SFE of CrCoNi solid-solution alloys serves to promote the formation of deformation nanotwins, which has been associated with the development of high strength, ductility, and toughness in crystalline alloys. (iii) This tunable SFE, which correlates with the negative or positive value of $\Delta E^{fcc-hcp}$, can also affect deformation-induced phase transformation from *fcc* to *hcp* phase. (iv) The predicted SFE are found to exhibit a large distribution in values that would be realized in an alloy solid solution, where the state of local chemical order varies heterogeneously throughout the sample. These unique aspects of stacking faults in CrCoNi solid solutions, resulting from the existence and variation of local chemical ordering, would be expected to influence the mechanisms of plastic deformation and hence the mechanical properties. The SFE effect in conventional crystalline alloys has been discussed (*SI Appendix, SI Text*). Compared with conventional alloys, however, the consequences of the unique aspects of planar fault energies for macroscopic deformation behavior remain incompletely understood for multicomponent HEAs. Thus, we believe that it is essential that further systematic studies be conducted on local chemical order as well as its role in influencing the mechanical deformation of HEAs in the future.

The findings from the present work highlight the general need to discern how critical the role of local chemical ordering is on the properties of other HEA systems (2, 32–35). It is important to note here that chemical order may affect not only the energies of stacking faults but also other critical defects, such as vacancies, interstitials, and twin boundaries, all of which could be similarly affected by tailoring the local chemical order to influence macroscopic mechanical properties. Strong variations in these defect energies will likely affect not only strength, ductility, and toughness but also resistance to high-temperature creep and even irradiation damage (36–38). Future research on structure–property relationships in these alloys should thus include consideration of the effects of local chemical order, to understand the degree to which chemical SRO can be used as an independent structural variable to guide alloy design and optimization. Our results thus highlight the possibility of tuning order in disorder to ultimately achieve the science-based design and optimization of new HEA systems with specifically desired combinations of macroscale mechanical properties.

Methods

DFT-Based Monte Carlo Simulations. The systems studied were equimolar CrCoNi ternary alloys in the *fcc* phase with lattice constant of 3.526 Å. For the Monte Carlo simulation, 18 independent supercells, containing 180 atoms each, were generated as special quasi-random structure (SQS) for initial starting points; SQS structures represent the best representative model of a random alloy in small systems with periodic boundary conditions (39). The temperature employed in the MC simulations was 500 K. Energy calculations were performed with the Vienna ab initio simulation package (40–42), using spin-polarized density functional theory, with a plane wave cutoff energy of 420 eV. Brillouin zone integrations were performed using Monkhorst–Pack

meshes with a $2 \times 2 \times 2$ grid (43). Projector augmented wave potentials (42) were employed with the Perdew–Burke–Ernzerhof generalized-gradient approximation for the exchange–correlation functional (44). Similar to the methods utilized in ref. 20, lattice MC simulations included swaps of atom types with the acceptance probability based on the Metropolis–Hastings algorithm (45). Finally, a conjugate-gradient algorithm was employed for structural relaxations at the end of the MC runs using a denser k -point mesh of $3 \times 3 \times 3$. We note that although the effect of spin polarization on the *fcc/hcp* energy difference in CrCoNi alloys with random substitutional configurations was found in ref. 18 to be relatively small, our DFT–MC simulations, performed with and without spin polarization included, led to differences in the averaged SRO parameter.

Local Chemical Order Parameter. Modified from the Warren–Cowley parameter (24), we defined the nonproportional number of local atomic pairs, $\Delta\delta_{ij}^k$, to quantify the chemical ordering around an atomic species for the first, second, and third nearest-neighbor shells, for which the corresponding coordination numbers are 12, 6, and 24, respectively. $\Delta\delta_{ij}^k$ was calculated as

$$\Delta\delta_{ij}^k = N_{0,ij}^k - N_{ij}^k, \quad [1]$$

where k denotes k th nearest-neighbor shells, N_{ij}^k is the actual (average) number of pairs between atoms of type j and type i in the k th shell, and $N_{0,ij}^k$ is the number of pairs that are proportional to the corresponding concentrations. In the case of a random solution, $\Delta\delta_{ij}^k = 0$. The total nonproportional number of all atomic pairs in the k th shell is $\Delta\delta_{sum}^k$.

1. Yeh JW, et al. (2004) Nanostructured high-entropy alloys with multiple principal elements: Novel alloy design concepts and outcomes. *Adv Eng Mater* 6:299–303.
2. Cantor B, Chang ITH, Knight P, Vincent AJB (2004) Microstructural development in equiatomic multicomponent alloys. *Mater Sci Eng A* 375:213–218.
3. Zhang Y, et al. (2014) Microstructures and properties of high-entropy alloys. *Prog Mater Sci* 61:1–91.
4. Pickering EJ, Jones NG (2016) High-entropy alloys: A critical assessment of their founding principles and future prospects. *Int Mater Rev* 61:183–202.
5. Miracle DB, Senkov ON (2016) A critical review of high entropy alloys and related concepts. *Acta Mater* 122:448–511.
6. Gludovatz B, et al. (2014) A fracture-resistant high-entropy alloy for cryogenic applications. *Science* 345:1153–1158.
7. Gludovatz B, et al. (2016) Exceptional damage-tolerance of a medium-entropy alloy CrCoNi at cryogenic temperatures. *Nat Commun* 7:10602.
8. Laplanche G, Kostka A, Horst OM, Eggeler G, George EP (2016) Microstructure evolution and critical stress for twinning in the CrMnFeCoNi high-entropy alloy. *Acta Mater* 118:152–163.
9. Laplanche G, et al. (2017) Reasons for the superior mechanical properties of medium-entropy CrCoNi compared to high-entropy CrMnFeCoNi. *Acta Mater* 128:292–303.
10. Zhang Z, et al. (2015) Nanoscale origins of the damage tolerance of the high-entropy alloy CrMnFeCoNi. *Nat Commun* 6:10143.
11. Zhang Z, et al. (2017) Dislocation mechanisms and 3D twin architectures generate exceptional strength–ductility–toughness combination in CrCoNi medium-entropy alloy. *Nat Commun* 8:14390.
12. Smith TM, et al. (2016) Atomic-scale characterization and modeling of 60° dislocations in a high-entropy alloy. *Acta Mater* 110:352–363.
13. Miao J, et al. (2017) The evolution of the deformation substructure in a Ni–Co–Cr equiatomic solid solution alloy. *Acta Mater* 132:35–48.
14. Hirth JP, Lothe J (1982) *Theory of Dislocations* (Wiley, New York).
15. Chowdhury P, Canadinc D, Sehitoglu H (2017) On deformation behavior of Fe–Mn based structural alloys. *Mater Sci Eng Rep* 122:1–28.
16. Zhang F, et al. (2017) Polymorphism in a high-entropy alloy. *Nat Commun* 8:15687.
17. Zhao SJ, Stocks GM, Zhang YW (2017) Stacking fault energies of face-centered cubic concentrated solid solution alloys. *Acta Mater* 134:334–345.
18. Niu C, LaRosa CR, Miao J, Mills MJ, Ghazisaeidi M (2018) Magnetically-driven phase transformation strengthening in high entropy alloys. *Nat Commun* 9:1363.
19. Ma E, Ding J (2016) Tailoring structural inhomogeneities in metallic glasses to enable tensile ductility at room temperature. *Mater Today* 19:568–579.
20. Tamm A, et al. (2015) Atomic-scale properties of Ni-based FCC ternary and quaternary alloys. *Acta Mater* 99:307–312.
21. Zhang FX, et al. (2017) Local structure and short-range order in a NiCoCr solid solution alloy. *Phys Rev Lett* 118:205501.
22. Ma Y, et al. (2018) Chemical short-range orders and the induced structural transition in high-entropy alloys. *Scr Mater* 144:64–68.
23. Widom M, Huhn WP, Maiti S, Steurer W (2014) Hybrid Monte Carlo/molecular dynamics simulation of a refractory metal high entropy alloys. *Metall Mater Trans A Phys Metall Mater Sci* 45:196–200.

Stacking Fault Energy Calculations. The average SFE, $\bar{\gamma}_{isf}$, and $\bar{\gamma}_{esf}$ of CrCoNi alloys have been calculated using supercell models, employing the same DFT methods described above. All of the SFE values were calculated using 360-atom supercells, as illustrated in Fig. 2 A–C, which were set up by sequentially stacking 12 close-packed (111) atomic planes. Two cases of sample initialization were implemented. The first case was constructed by replicating the 180-atom configurations in the z direction normal to the stacking fault plane, including those at four different states, *CH_0*, *CH_1*, *CH_2*, and *CH_F*; for each state, there were 108 stacking faults under study, extracted from 18 independent samples, whose six planes were all considered for each configuration by shifting the stacking fault to the middle of the constructed supercells. The second case was for the directly as-assigned 360-atom configuration with random solid solution, representing 108 independent configurations in total. The atomic configurations for each sample were structurally relaxed in the three directions. Next, an ISF and ESF were created in a stacking sequence of *ABCABC|BCABCA* (Fig. 2B) and *ABCABC|B|ABCAB* (Fig. 2C), respectively. The SFE was obtained from the energy difference of the two optimized structures normalized by the area of the stacking fault.

ACKNOWLEDGMENTS. This work was supported by the Mechanical Behavior of Materials Program (KC13) at the Lawrence Berkeley National Laboratory, funded by the US Department of Energy, Office of Science, Office of Basic Energy Sciences, Materials Sciences and Engineering Division, under Contract DE-AC02-05CH11231. The study made use of resources of the National Energy Research Scientific Computing Center, which is also supported by the Office of Basic Energy Sciences of the US Department of Energy under Contract DE-AC02-05CH11231.

24. Warren BE (1990) *X-Ray Diffraction* (Dover Publications, New York).
25. Zhang YH, et al. (2017) The origin of negative stacking fault energies and nano-twin formation in face-centered cubic high entropy alloys. *Scr Mater* 130:96–99.
26. Huang H, et al. (2018) Critical stress for twinning nucleation in CrCoNi-based medium and high entropy alloys. *Acta Mater* 149:388–396.
27. Nohring WG, Curtin WA (2017) Dislocation cross-slip in fcc solid solution alloys. *Acta Mater* 128:135–148.
28. Ma D, Grabowski B, Kormann F, Neugebauer J, Raabe D (2015) Ab initio thermodynamics of the CrCrFeMnNi high entropy alloy: Importance of entropy contributions beyond the configurational one. *Acta Mater* 100:90–97.
29. Olson GB, Cohen M (1976) A general mechanism of martensitic nucleation: Part I. General concepts and the FCC \rightarrow HCP transformation. *Metall Trans A Phys Metall Mater Sci* 7A:1897–1904.
30. Pradeep KG, et al. (2013) Atomic-scale compositional characterization of a nanocrystalline AlCrCuFeNiZn high-entropy alloy using atom probe tomography. *Acta Mater* 61:4696–4706.
31. Ozdol VB, et al. (2015) Strain mapping at nanometer resolution using advanced nanobeam electron diffraction. *Appl Phys Lett* 106:253107.
32. Santodonato LJ, et al. (2015) Deviation from high-entropy configurations in the atomic distributions of a multi-principal-element alloy. *Nat Commun* 6:5964.
33. Li Z, Pradeep KG, Deng Y, Raabe D, Tasan CC (2016) Metastable high-entropy dual-phase alloys overcome the strength–ductility trade-off. *Nature* 534:227–230.
34. Senkov ON, Miller JD, Miracle DB, Woodward C (2015) Accelerated exploration of multi-principal element alloys with solid solution phases. *Nat Commun* 6:6529.
35. Claudia M, et al. (2015) Criterion for predicting the formation of single-phase high-entropy alloys. *Phys Rev X* 5:011041.
36. Zhang Y, et al. (2015) Influence of chemical disorder on energy dissipation and defect evolution in concentrated solid solution alloys. *Nat Commun* 6:8736.
37. Granberg F, et al. (2016) Mechanism of radiation damage reduction in equiatomic multicomponent single phase alloys. *Phys Rev Lett* 116:135504.
38. Lu C, et al. (2016) Enhancing radiation tolerance by controlling defect mobility and migration pathways in multicomponent single-phase alloys. *Nat Commun* 7:13564.
39. Zunger A, Wei S, Ferreira LG, Bernard JE (1990) Special quasirandom structures. *Phys Rev Lett* 65:353–356.
40. Kresse G, Hafner J (1993) Ab initio molecular dynamics for liquid metals. *Phys Rev B Condens Matter* 47:558–561.
41. Kresse G, Hafner J (1994) Ab initio molecular-dynamics simulation of the liquid-metal–amorphous-semiconductor transition in germanium. *Phys Rev B Condens Matter* 49:14251–14269.
42. Kresse G, Joubert D (1999) From ultrasoft pseudopotentials to the projector augmented-wave method. *Phys Rev B Condens Matter Mater Phys* 59:1758–1775.
43. Monkhorst H, Pack J (1976) Special points for Brillouin-zone integrations. *Phys Rev B* 13:5188–5192.
44. Perdew JP, Burke K, Ernzerhof M (1996) Generalized gradient approximation made simple. *Phys Rev Lett* 77:3865–3868.
45. Hastings WK (1970) Monte Carlo sampling methods using Markov chains and their applications. *Biometrika* 57:97–109.